Nanoscale Horizons

Ultra-sensitive Colloidal Quantum Dot Infrared Photodiode Exceeding 100,000% of External Quantum Efficiency via Photomultiplication.

Journal:	*Nanoscale Horizons*
Manuscript ID	NH-CMT-10-2023-000456.R1
Article Type:	Communication
Date Submitted by the Author:	26-Dec-2023
Complete List of Authors:	Jung, Byung Ku; Korea University, Park, Taesung; Korea University - Seoul Campus, Materials Science and Engineering Choi, Young Kyun; Korea University, Material science and engineering Lee, Yong Min; Korea University - Seoul Campus Kim, Tae Hyuk; Korea University, Electrical Engineering Seo, Bogyeom; University of California San Diego, Department of Electrical and Computer Engineering Oh, Seongkeun; Korea University Shim, Jae Won; Korea University, Electrical Engineering Lo, Yu-Hwa; University of California San Diego, Department of Electrical and Computer Engineering Ng, Tse Nga; University of California San Diego, Oh, Soong Ju; Korea University, Department of Materials Science and Engineering

SCHOLARONE™
Manuscripts

PbS colloidal quantum dots have widely considered attractive IR absorbing material due to their programmable absorption range from visible to short wavelength IR, high intrinsic absorption coefficient ($>10^{4}$ cm $^{-1}$), and high electron and hole mobility ($>10^{-1}$ cm $V^{-1}s^{-1}$). While PbS CQD thin film IR photodiode (PD) exhibits high performance such as external quantum efficiency of 80 % comparable to commercial infrared photodetectors, further improvement is required for the potential applications in quantum communications, bioimaging, Lidar, etc. In this work, we present highly efficient PbS CQDs-based multiplication-type photodiode exceeding 100,000 % using the double charge accumulation strategy. The charge accumulations strategy was achieved by utilization of long ligand encapsulated NC thin films, inducing band-bending induced tunneling based photomultiplication. Combinatorial analysis indicate a direct correlation between accumulated charge density and the photomultiplication process. We believed that our findings will not only serve as a source of inspiration for improving the EQEs of photomultiplication-type photodiode but also significantly contribute to next generation quantum optics and optoelectronics.

ARTICLE

Ultra-sensitive Colloidal Quantum Dot Infrared Photodiode Exceeding 100,000% of External Quantum Efficiency via Photomultiplication.

Received 00th January 20xx,
Accepted 00th January 20xx

DOI: 10.1039/x0xx00000x

Byung Ku Jung[a], Taesung Park[a], Young Kyun Choi[a], Yong Min Lee[a], Tae Hyuk Kim[b], Bogyeom Seo[c], Seongkeun Oh[a], Jae Won Shim[b], Yu-hwa Lo[c], Tse Nga Ng[c], Soong Ju Oh*

In this study, we present ultrasensitive infrared photodiodes based on PbS colloidal quantum dot (CQD) operating on a double photomultiplication strategy that utilizes the accumulation of both electron and hole carriers. While electron accumulation was induced by ZnO trap states that were created by treatment in a humid atmosphere, hole accumulation was achieved using a long-chain ligand that increased the barrier to hole collection. Interestingly, we obtained the highest responsivity in photo-multiplicative devices with the long ligands, which contradicts the conventional belief that shorter ligands are more effective for optoelectronic devices. Using these two charge accumulation effects, we achieved an ultrasensitive detector with a responsivity above 7.84×10^2 AW^{-1} and an external quantum efficiency above 10^5% in infrared region. We believe that the photomultiplication effect has great potential for surveillance system, bioimaging, remote sensing, and quantum communication.

Introduction

Infrared (IR) photodetectors are in great demand owing to their applications in light detection and ranging (LiDAR) sensors, optical communication, driverless vehicles, and security systems.[1–4] In particular, photomultiplication-type IR photodiodes (PDs) have been reported to have great advantages in detecting weak light without a photocurrent amplification system, yielding great potential for advanced applications[5–9] such as IR-to-visible upconversion, bioimaging, remote sensing, and quantum communication. To date, narrow-bandgap IR-absorbing materials, such as epitaxially grown III-V semiconductors (InGaAs and InSb) or $Hg_{1-x}Cd_xTe$, have been used to effectively absorb IR radiation and achieve highly sensitive photomultiplication-type IR PDs.[10–12] Unfortunately, these materials require high-temperature or vacuum processing; these processes increase the cost of IR photodetectors and limit their application in industrial and military fields.
Colloidal quantum dots (CQDs) are promising next-generation materials for optoelectronic devices because of their low-temperature solution-based processability[13–15] coupled with high adsorption and crystalline robustness, which allow them to be directly deposited on silicon readout integrated circuits.[16,17] In particular, lead chalcogenide (PbE) (PbS and PbSe) CQDs have been used as IR absorbing materials owing to their widely programmable absorption range from visible to short wavelength IR coupled with their high intrinsic absorption coefficient (>10^4 cm $^{-1}$) and high electron and hole mobility (>10^{-1} cm $V^{-1}s^{-1}$).[18–25] The physical properties of PbS CQD thin films have been precisely controlled at the material level, and numerous studies have attempted to increase the surface ligand density to eliminate dangling bonds that generate deep mid-gap states and capture photogenerated carriers. The energy level of the PbS CQD thin film has been modified by tailoring its stoichiometry to minimize the energy barrier between the layers that constitute the optoelectronic devices and induce directional carrier diffusion. Various deposition methods such as spin-, blade-, and meniscus-guided coatings have been developed to fabricate densely packed PbS CQD thin films[26–28]. As a result of these efforts, PbS CQD-based optoelectronics have reported outstanding performance in various devices such as phototransistors, photoconductors, and PDs. In particular, PbS CQD-based IR PDs also exhibit high external quantum efficiency (EQE) (>50%) and detectivity (>10^{12} Jones) in the IR range. Although various PbS CQD-based optoelectronics have been reported, only a few studies have reported photomultiplication-type quantum-dot photodiodes (PM-QPDs),[29,30] and further improvement in their responsivity is still needed.

In this work, we present a double photomultiplication strategy that induced the accumulation of both electron and hole carriers and report a sensitive PM-QPD. We designed PM-QPD devices where the charge accumulations occurred at electron-/hole-transporting layer (ETL/HTL) by electron and hole carriers, respectively. Subsequently, the band bending amplifies photogenerated carriers by accelerating charge injection by tunneling from electrodes above a threshold voltage. Electron

[a] Department of Materials Science and Engineering, Korea University, 145, Anam-ro Seongbuk-gu Seoul 02841, Republic of Korea.
[b] School of Electrical Engineering, Korea University, Seoul 02841, Republic of Korea.
[c] Department of Electrical and Computer Engineering, University of California San Diego, La Jolla, California 92093-0407, United States.
† Electronic Supplementary Information (ESI) available: See DOI: 10.1039/x0xx00000x

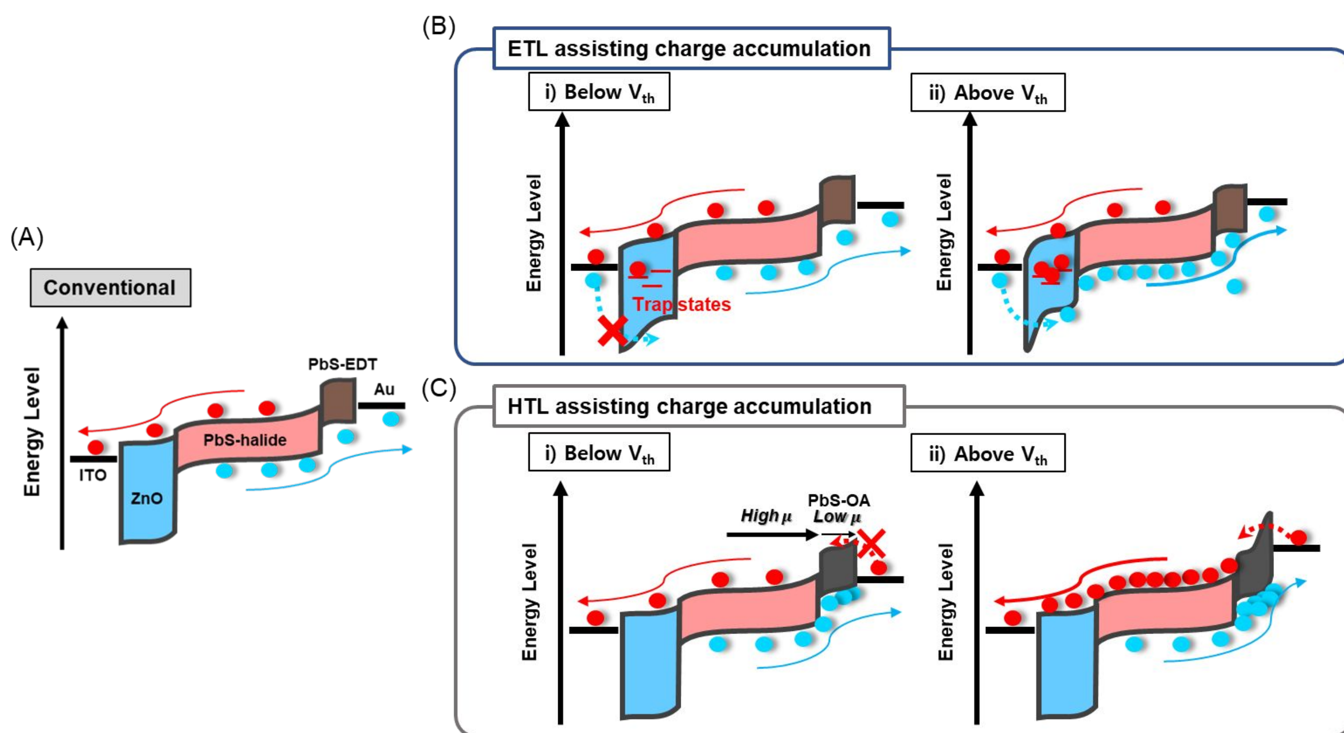

Figure 1. Schematic of carrier dynamics in (A) conventional PbS CQDs-based IR PD and (B) ETL and (C) HTL-assisted charge accumulation strategies.

accumulation was realized through trap states induced by exposing ZnO thin film (ETL) in a humid atmosphere, resulting in enhancing energy-level bending and tunneling of hole carriers from the bottom electrode. Hole accumulation was initiated by a bottleneck effect originating from the difference in hole mobility between the IR absorbing layer and the oleic acid (OA) passivated PbS thin film (HTL); Although it is commonly believed that shorter ligands are more effective for optoelectronic devices, we intentionally utilized an OA passivated layer (PbS-OA) to efficiently hinder the hole carrier extraction from the HTL to the electrode and to accumulate the holes towards energy-level bending. This design leads to electrons tunneling from top electrode and enlarges the multiplication effect. Combinational studies of structural, optical, and electrical analyses were conducted to demonstrate the double photomultiplication strategy. The optimized PM-QPD achieves a EQE (> 10^5%), which is the highest EQE among reported PM-QPDs to the best of our knowledges.

Results and discussion,

The ~4 nm size of PbS CQDs were synthesized *via* hot injection method. For IR absorbing layer, halide ligand passivated PbS QD thin films (PbS-halide) were used. For HTL, ethane-1,2-dithiol (PbS-EDT) and oleic acid passivated (PbS-OA) PbS QD thin films were prepared, while for ETL ZnO thin film were used, as detailed in **Experimental Section**. Their structural and physical properties were analyzed using transmission electron microscopy, UV-vis, and ultraviolet photoelectron spectroscopy in **Figure S1**. In **Figure 1A**, conventional PbS-QPD with an indium tin oxide (ITO)/ZnO/PbS-halide/PbS-EDT/Au structure is shown, and the fabrication processes of one are described in the Experimental section. In the conventional PbS-QPD structure, photogenerated carriers are extracted without any multiplication effects. In this study, we introduced a double photomultiplication strategy via the ETL and HTL to assist in charge accumulation, as shown in **Figure 1B and 1C**, respectively. First, the density of trap states at the ETL was precisely controlled by treatment of the ZnO thin films in a humid atmosphere. These trap states capture electron carriers and form a local electrical field that additionally accelerates band bending with an external bias. Above the threshold voltage V_{th}, hole carriers are injected from the ITO electrode via a tunneling effect from the ITO electrode (**Figure 1B**). Second, we intentionally designed a large difference in the hole carrier mobility between the HTL and the PbS halide to accumulate hole carriers by using PbS-OA as HTL. Considering that the carrier velocity is proportional to the mobility and external bias, more hole carriers accumulate in the HTL when a higher external voltage is applied. Above V_{th}, the local electrical field triggered electron carrier tunneling from the Au electrode (**Figure 1C**).

To induce defect states in the ZnO layer that capture electron carriers, we performed humidity treatment on the as-synthesized ZnO thin films. ZnO thin films were deposited by spin coating under dry conditions (ZnO-pristine) (relative humidity < 20%), and then, ZnO-pristine was stored in a humid chamber (ZnO-Hydrated) (relative humidity > 80%) (**Figure 2A**). To analyse the effect of the humidity treatment on the optical properties of the ZnO thin films, the FTIR spectra of the ZnO thin films before (ZnO-pristine) and after treatment (ZnO-Hydrated) were measured (**Figure 2B**). Several peaks were observed at 2800–

This journal is © The Royal Society of Chemistry 20xx
Please do not adjust margins

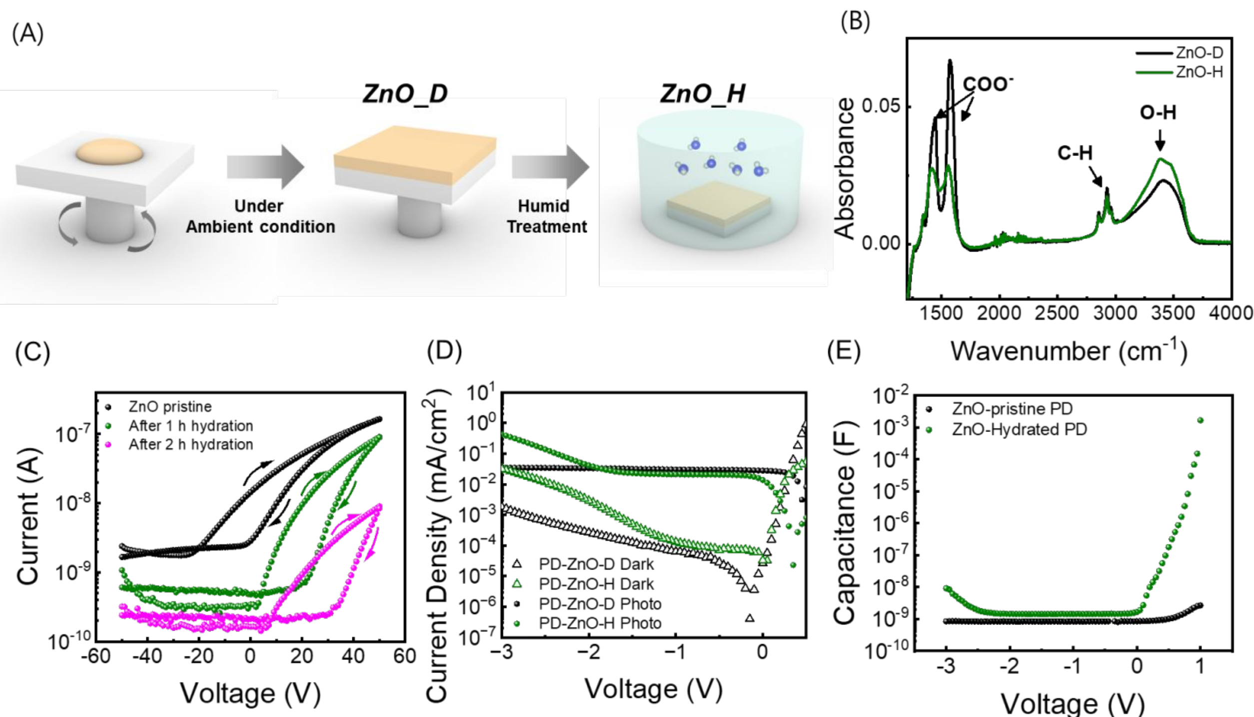

Figure 2. (A) Fabrication process of the ETL without (ZnO-pristine) and with humidity treatment (ZnO-Hydrated). (B) Fourier-transform IR spectroscopy (FTIR) spectra of ZnO-pristine and ZnO-Hydrated. (C) The source-drain current (I_{DS}) vs gate voltage (V_G) curve of the ZnO thin film-based FET transistor by humidity treatment. (D) Current density-voltage (*J-V*) of PbS QPDs using ZnO-pristine and ZnO-Hydrated measured under the dark state and 980 nm illumination with an intensity of 13 uW/cm^2. (E) Capacitance-voltage curves (*C-V*) of PbS QPDs.

3000 cm^{-1} (C–H stretching) and two peaks at 1571 cm^{-1} and 1417 cm^{-1} (COO^-) stemming from the zinc acetate precursor.[31–33] In addition, a broad O–H stretching peak at 3500 cm^{-1} corresponds to the OH^- ligand of the ZnO nanoparticles (NPs). After humidity treatment, while the intensities of the peaks related to acetates decreased, the O–H stretching peak increased, as observed in the FTIR spectrum of ZnO-Hydrated.[34] These results indicate the disappearance of acetate molecules located on the ZnO NP surface owing to the sintering effect and the attachment of water molecules on the surface of the ZnO NPs. UV-vis and photoluminescence (PL) results (**Figure S2**) discussed in Supporting Information Note 1.

To measure the effect of humidity treatment on the electrical properties of the ZnO thin films, we measured the electron mobility using a field-effect transistor (FET) (**Figure 2C**).[34] The transfer curve of pristine ZnO exhibited a turn-on voltage at V_G = 15.9 V, and the calculated electron mobility was 6.45× 10^{-4} cm^2 V^{-1} s^{-1} in the saturation regime. After 1 h of humidity treatment, the transfer curve revealed a large increase in the turn-on voltage to 36.1 V, a slight decrease of the electron mobility to 4.97 × 10^{-4} cm^2 V^{-1} s^{-1}, and a slight increase of the device hysteresis (**Figure S3**). After 2 h of humidity treatment, the turn-on voltage and the mobility became 42.6 V and 3.67 × 10^{-5} cm^2 V^{-1} s^{-1}, respectively. Considering that the turn-on voltage in n-type TFTs positively shifts when the doping level increases, humidity treatment decreases both the charge carrier mobility and density in ZnO thin films. We attributed these results to the formation of defect trap states in ZnO films under humidity treatment.

We fabricated two different PbS QPDs using ZnO-pristine and 1 h of humidity treated ZnO-Hydrated as the ETL, denoted as PD with ZnO-pristine and PD with ZnO-Hydrated, respectively. It should be noted that long time humidity treatment (>2h) deteriorate the photodiode performance as it creates too many defects and reduce the mobility (**Figure S3**). In **Figure 2D**, the *J-V* curves of the two devices are shown in the dark and under illumination. PD with ZnO-pristine exhibited a saturated photocurrent density as the value of the reverse bias increased. In contrast, PD with ZnO-Hydrated (1h) exhibited a saturated photocurrent density at a low reverse bias, but a rapid increase in photocurrent density was observed above the threshold voltage ($V_{th\text{-}J}$). $V_{th\text{-}J}$ was calculated from the derivative of photocurrent density with respect to the voltage versus voltage graph (dJ_{photo}/dV-V) and found to be −1.8 V. To further investigate the reason of photomultiplication in the devices, *C-V* curves were measured from −3 V to 1 V. While PD with ZnO-pristine exhibited a constant capacitance independent of the applied reverse bias, PD with ZnO-Hydrated initially showed a constant capacitance, but a rapid increase occurred above threshold voltage, which is similar to its *J-V* curve (**Figure 2E**). The threshold voltage of capacitance ($V_{th\text{-}C}$) was confirmed from the derivative of the capacitance with respect to the voltage versus voltage graph (dC/dV-V) and found to be −1.9 V (**Figure S4**). It is important to note that the $V_{th\text{-}C}$ of PD with ZnO-Hydrated was similar to $V_{th\text{-}J}$ of PD with ZnO-Hydrated, with a slight difference, implying that the origin of photocurrent amplification was closely related to charge accumulation in the device.

This journal is © The Royal Society of Chemistry 20xx

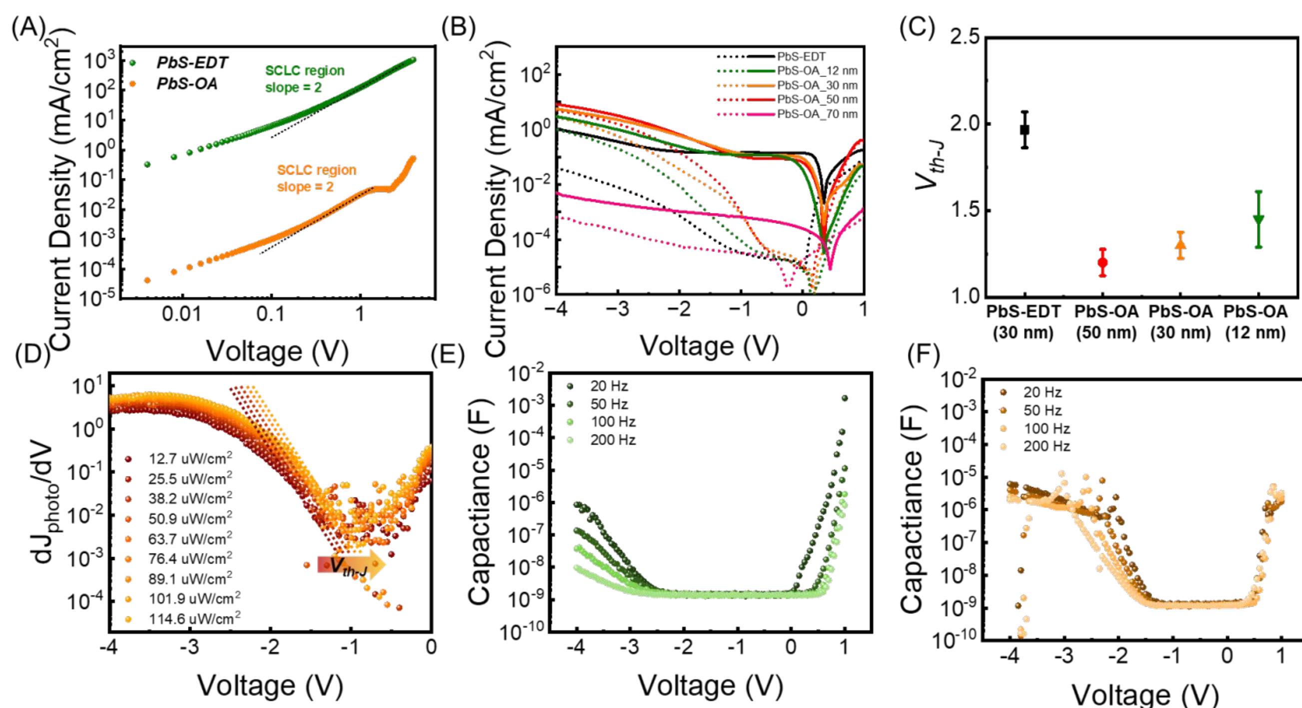

Figure 3. (A) Space charge limited current (SCLC) results of PbS-EDT and PbS-OA hole-only devices. (B) *J-V* curves of PDs with PbS-EDT and PbS-OA (12, 30, 50, 70 nm) under dark and 980 nm laser illumination with a 130 μW/cm² intensity, and the (C) calculated $V_{th\text{-}J}$. (D) dJ_{photo}/dV-V curve of PD with PbS-OA (30 nm) measured under different light intensities. Frequency dependent *C-V* curves of the PbS QPD using (E) PbS-EDT (30 nm) and (F) PbS-OA (30 nm) as HTLs

To maximize the band-bending-induced tunneling and photomultiplication effects, we designed a device geometry with large hole carrier accumulation at the HTL. For efficient hole carrier accumulation at the HTL, low-mobility HTL materials were chosen to increase the hole mobility difference between the PbS halide and HTL layers. The carrier mobility in QD films is inversely proportional to the ligand length and the number of carbon chains in ligands. Therefore, instead of the conventional EDT (2 carbon) ligand, we introduce an oleic acid (18 carbon)-passivated PbS CQD thin film as the HTL to maximize the hole mobility difference between the PbS-halide (0 carbon) and HTL. From the transfer curve of the FET device, the hole carrier mobility of PbS-EDT was determined to be 2.57 × 10^{-4} cm^2 V^{-1} s^{-1} in the saturation regime, while that of PbS-OA could not be measured because of its considerably low mobility (**Figure S5**). To further examine the hole carrier mobilities of PbS-EDT and PbS-OA, the vertical structures with hole-only devices (ITO/PEDOT:PSS/HTL/MoO_3/Au) were prepared, and space charge limited measurements (SCLC) were conducted (**Figure 3A**). The *J-V* curve measured from the SCLC was fitted using the Mott-Gurney law.[2,35] The hole mobility of each QD film was determined from the SCLC region (slope = 2). The hole mobilities of PbS-EDT and PbS-OA were found to be $\mu_{h,EDT}$ = 1.6 × 10^{-4} cm^2 V^{-1} s^{-1} (similar to the FET results) and $\mu_{h,OA}$ = 7.95 × 10^{-10} cm^2 V^{-1} s^{-1}.

To measure the effect of different HTL layers on the device performance, ITO/ZnO-pristine/PbS-halide/PbS-EDT/Au (PD with PbS-EDT) and ITO/ZnO-pristine/PbS-halide/PbS-OA/Au (PD with PbS-OA) photodiodes with varying PbS-OA thickness (12, 30, 50, and 70 nm) were prepared. J-V characteristics of the PD with PbS-EDT and PbS-OA are shown in Figure 3B. Below the $V_{th\text{-}J}$ of the PD (−1.3 V), the PD with PbS-OA shows a lower illuminated current density value compared to the PD with PbS-EDT because the low hole mobility of the PbS-OA hinders the extraction process of photogenerated hole carriers (**Figure S6**). In contrast, above the $V_{th\text{-}J}$, the PD with 12, 30, and 50 nm PbS-OA exhibited a large photomultiplication effect and achieved a higher illuminated current density than that with PbS-EDT. As PbS-OA has low hole mobility, holes are accumulated in this layer, inducing band-bending and subsequently tunneling under high voltage. As PbS-OA is the most insulating layer in the PD, the voltage drop occurs in PbS-OA, inducing high electric fields above 2.5x10^8 V/cm. Therefore, despite the low hole mobility in PbS-OA, the charge transport by tunneling between OA-capped PbS QDs is allowed under high voltage, leading to a huge photocurrent density.

As the thickness of PbS-OA increases from 12 to 50 nm, more charges accumulate, leading to higher band bending-induced tunneling currents. At a thickness of 12 nm, the charge accumulation is low so that band bending-induced tunneling is low, leading to low photomultiplication. At a thickness of 50 nm, an excessive number of carriers are accumulated, leading to an excessively high dark current. As a result, the photo/dark current ratio is low, as discussed in detail in **Figure S7**. Therefore, the PD with PbS-OA is optimized with a PbS-OA thickness of 30 nm. Notably, when the PbS-OA is too thick (above 70 nm), this layer becomes completely insulating. As band bending occurs

This journal is © The Royal Society of Chemistry 20xx

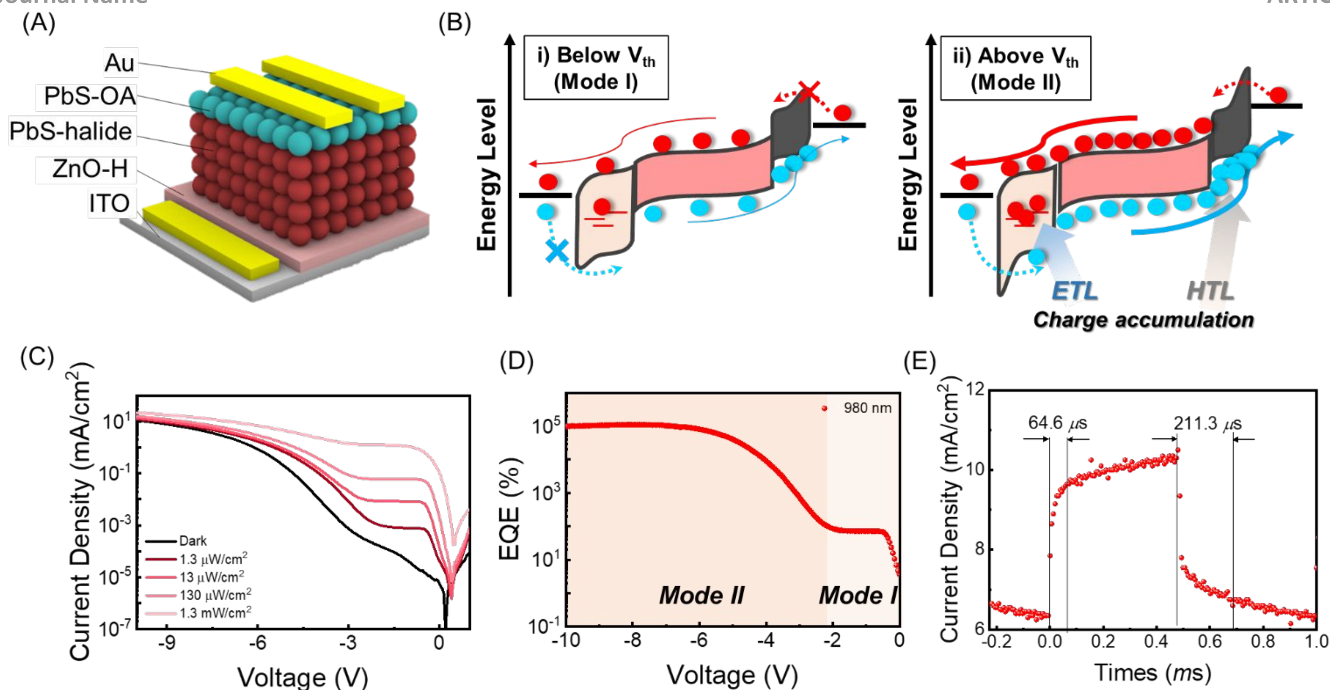

Figure 4. (A) Schematic of the PM-QPD structure and (B) charge accumulation assisted photomultiplication mechanism of PM-QPD. (C) *J-V* curve of PM-QPD under a 980 nm laser with varying light intensity from 1.3 μW cm^{-2} to 1.3 mW cm^{-2}. (D) EQE versus voltage graph under 980 nm with an intensity of 1.3 μW cm^{-2}. (E) Response speed of PM-QPD at a –10 V bias.

only at the interface and the main body of PbS-OA is insulating, tunneling is not allowed, yielding low dark current and photocurrent, as seen in **Figures 3B** and **S8A**.

To further investigate the photomultiplication, thickness, light intensity, and temperature dependent electrical measurements were performed. As seen in **Figure 3C**, $V_{th\text{-}J}$ of PD with PbS-OA is inversely proportional to the thickness of PbS-OA, this indicates that the more hole carriers accumulated by thicker PbS-OA accelerate tunneling and photomultiplication phenomenon. The thickness of PbS-OA was optimized as 30 nm, as detailed in **Figure S7** and Supporting Information Note 2. In addition, $V_{th\text{-}J}$ gradually decreases as temperature increases (**Figure S8B**); At higher temperature, the mobility difference becomes extended in coincide with the great increment of mobility of PbS-halide, enhancing hole carrier accumulation. As intensity of light increases, $V_{th\text{-}J}$ is decreased and this also can be rationalized that larger amount of photogenerated carriers assist hole accumulation (**Figure S8C and 3D**). These analyses strongly support that hole mobility difference induced charge accumulation and band bending in HTL leads to large photomultiplication.

The charge accumulation in PD with PbS-EDT and PbS-OA was measured using frequency dependent *C-V* curve from −4 V to 1 V from 20 Hz to 200 Hz (**Figure 3E and 3F**). From these results, we calculated the changes of $V_{th\text{-}C}$ by detecting frequency. In the case of PD with PbS-EDT, the measured capacitance at the accumulation region significantly decreased, and its $V_{th\text{-}C}$ changed from −1.9 V to −2.5 V as the applied frequency increased from 20 Hz to 200 Hz (**Figure S9A**). This large frequency-dependent capacitance shift in this low frequency range (<10^3 Hz) describes the origin of ETL-assisted carrier accumulation as deep interfacial defect states caused by humidity treatment.[36] In contrast, $V_{th\text{-}C}$ of PD with PbS-OA exhibited a frequency independent behavior in this range, which changed minimally at −1.3 V (**Figure S9B**).

Figure 4A shows the structure of our PM-QPD designed via a double photomultiplication strategy. In **Figure 4B**, the PD mode (Mode I) and PM mode (Mode II) are commonly observed below and above the V_{th}, respectively. Below V_{th}, PM-QPD exhibited photodiode behaviors, including no dramatic photocurrent density increase with an increase in the reverse voltage value. In contrast, above V_{th} (mode II), sufficient voltage is applied, and charge-accumulation and tunneling occur, leading to photomultiplication. In **Figure 4C**, the *J-V* curves of PM-QPD monitored under a dark state and various intensities of 980-nm-light are shown. A rapid increase in the photocurrent density and photomultiplication effect occurred above V_{th}, which is attributed to the band bending induced tunneling and carrier multiplication under high voltage and electrical field. We observed two clearly divided regions of Mode I and Mode II. In **Figure 4D**, PM-QPD exhibited constant EQE as the reverse bias increased in Mode I (0 ~ –2 V), whereas the EQE rapidly increased above 10^5% in Mode II (–2 ~ –10 V).

To further analyze the operating mechanisms of Modes I and Mode II, we replotted the photocurrent density versus light intensity curves in **Figure S10**. In Mode I, PM-QPD shows linear growth ($J_{ph} \propto P^n$, $n \cong 1$) with the incident optical power, n =1.03 at – 1 V, implying that photogenerated carriers were extracted by the built-in potential. On the other hand, in Mode II, PM-QPD shows sublinear growth ($J_{ph} \propto P^n$, $n < 1$) with the incident power,

n =0.31 at – 10 V. These low n values reveal strong a photogain effect and dominant contribution of photogating to the total photocurrent generation, where photoexcited carriers are trapped in localized states and generate a local electric field.[37] In addition, using a 1 kHz laser pulse, the response time of PM-QPDs was measured at –1 V, –4 V, and –10 V. The rise-time was measured from 10% to 90% of the highest value, and the fall-time was conversely measured from 90% to 10%. Compared to other types of photomultiplication devices such as phototransistors (> 10 ms)[38,39], our PM-QPD exhibited a faster response speed with rise- and fall-times of 12.8 μs/28.8 μs at –1 V (Mode I), 28.8 μs/100 μs at –4 V, and 64.6 μs/211.3 μs at –10 V (Mode II) (**Figure S11 and 4E**). More detailed characterization regarding device stability is presented in **Figure S12**.

To quantitatively measure the performance of the PM-QPD, the calculated EQE spectrum is depicted in **Figure S13**. In Mode I, regardless of the wavelength, PM-QPD exhibited an EQE below 10^2%. On the other hand, as the applied bias increased in Mode II, the EQE of PM-QPD was largely multiplied and reached 10^5% above a bias of –8 V. Above – 10 V, PM-QPD was largely deformed and lost their performance. Record performance was achieved at – 10 V with responsivity of 7.84×10^2 AW^{-1} and EQE of 1.46×10^5%. These are the highest responsivity and EQE values (>10^5%) among previously reported PM-QPDs, which were obtained by chemical treatment of ZnO and the utilization of QDs with long ligands (**Table S1**).

Conclusions

We developed an efficient PM-QPD using a double photomultiplication strategy. Through humidity treatment, we precisely controlled the interfacial defect density on the ETL, thereby accumulating electron carriers. Contrary to the conventional thoughts, long-chain OA ligand passivated CQDs were used as HTL and induced a large carrier mobility difference and triggered hole-carrier accumulation, resulting in a large photomultiplication effect. These charge accumulations were further investigated using capacitance and current-voltage measurements. The fabricated PM-QPD exhibited two distinct operation modes, the PD and PM modes. At PM modes, they reported the ultra-high EQE of 1.46×10^5% under 980 nm. This photomultiplication effect can be applied to advanced future technologies such as quantum communication, which requires the detection of signal photons under ambient conditions.

Experimental

Materials: Ammonium acetate (NH_4Ac), lead(II) oxide (PbO) (99.999%), zinc acetate dihydrate, lead(II) iodide (PbI_2), oleic acid (OA) (90%), lead(II) bromide ($PbBr_2$), potassium hydroxide (KOH), bis(trimethylsilyl)sulfide (TMS_2) (98%), n-octane (99%), dimethylformamide (DMF), 1-octadecene (ODE) (90%), 1,2-ethanedithiol (EDT) (98%), butylamine, and acetonitrile were purchased from the Sigma-Aldrich Co. All reagents were used without further purification.

Synthesis of ZnO NPs and PbS QDs: ZnO NPs were synthesized using a slightly modified method from a previous study.[40] The Zn precursor was prepared by dissolving zinc acetate dihydrate (2.95 g) in methanol (125 mL) and heating the solution to 60 °C. A KOH solution (1.48 g in 65 mL of methanol) was slowly injected into the Zn precursor. The mixture was stirred at 60 °C for 2.5 h and then cooled to room temperature. The obtained ZnO NPs were purified thrice using pure methanol. Purified ZnO NPs were collected in chloroform (70 mg mL^{-1}).

PbS QDs were synthesized using a previously reported hot-injection method.[22] A solution of OA (3 mL), PbO (0.9 g), and ODE (20 mL) was degassed in a 100 mL three-neck flask for 2 h at 110 °C. Next, the solution was heated to 120 °C under a nitrogen atmosphere. The sulfur precursor (240 μL of TMS_2 in 8 mL of ODE) in a 10 mL syringe was injected into the flask and then cooled to room temperature via natural cooling. The synthesized QDs were purified three times using acetone and ethanol. Finally, the QDs were dispersed in octane (50 mg mL^{-1}).
A solution exchange process was conducted to cap the PbS QDs with lead halide ligands using a previously reported method with slight modifications.[41] Lead halides (0.46 g of PbI_2 and 0.07 g of $PbBr_2$) and NH_4Ac (0.03 g) were dissolved in DMF (10 mL). Subsequently, the synthesized QDs (10 mL, 10 mg mL^{-1}) were vigorously mixed with the DMF solution for 2 min. The ligand-exchanged QD solution was washed three times with octane and centrifuged in toluene. The precipitated QDs were collected using butylamine (200 mg mL^{-1}).

Fabrication of the NIR photodetector: ITO-deposited glass was sequentially cleaned with acetone, isopropanol, and deionized water for 5 min via sonication. The ITO glass was then treated with UV-ozone for 20 min and spin coated with ZnO NPs at 2500 rpm for 30 s under dry conditions. To obtain a dense ZnO layer, a ZnO thin film was annealed for 10 min at 80 °C (ZnO-pristine). For humidity treatment, the ZnO-pristine thin film was placed in a humidity chamber (relative humidity > 80%) for 1 h. The solution-exchanged PbS QDs were then spin-coated onto the ZnO thin film at 2500 rpm for 30 s. Next, the PbS-OA layer was deposited by spin-coating with the as-synthesized OA-capped PbS QDs at 2500 rpm for 30 s for the fabrication of a 30-nm-thick PbS-OA layer. The PbS-EDT layer was deposited using the solid exchange method. An EDT solution (0.02 vol% in acetonitrile) was applied to the OA-capped PbS QD films for 30 s to exchange the ligands. The films were washed three times with acetonitrile to eliminate residues from the ligand exchange process. An 100-nm-thick Au top electrode was deposited on the hole transport layers via thermal evaporation. The area of the device was 4 mm^2.

Characterization: An LCR meter (model 4100, Wayne Kerr) and a probe station (MST-4000A, MSTECH) were used to measure

This journal is © The Royal Society of Chemistry 20xx

the capacitance-voltage curve of the PbS QDPD. The current density-voltage characteristics were measured using a source meter (Keithley 2400, Tektronix). UV-Vis (Cary5000, Agilent Technologies) and FTIR (Model LabRam ARAMIS IR2, Horiba Jobin Yvon) spectroscopy techniques were used to analyze the optical properties of the ZnO NPs and PbS CQD thin films. In addition, a high-resolution transmission electron microscope (Tecnai G2 F30, FEI, Korea Basic Science Institute) was used to analyze the structures of the ZnO NPs and PbS CQDs. The local atomic structures of the ZnO NPs were evaluated using X-ray absorption spectroscopy. EQE spectra were obtained using a K3100 EQX quantum efficiency measurement system (McScience). Monochromated white light from a xenon lamp was mechanically chopped at a frequency of 300 Hz.

To quantify the performance of the PM–QPDs, their responsivity (R) and EQE was calculated using the following equations:[42,43]

(1) $J_{photo} = J_{illuminated} - J_{dark}$, and

(2) $R = \frac{J_{photo}}{P}$, and

(3) $EQE = \frac{hcR}{e\lambda}$

,where $J_{illuminated}$ and J_{dark} are the current density values in the illuminated and dark states, respectively; A is the active area of the device; P is the light power intensity; and q is the electron charge [44].

Author Contributions

Byung Ku Jung: Conceptualization, Methodology, Formal analysis, Investigation, writing – original draft, Writing – review & editing. *& Taesung Park:* Conceptualization, Methodology, Visualization, *Young Kyun Choi*: Formal analysis, writing – original draft, Writing – review & editing. *Yong Min Lee*: Methodology, Data curation, *Seongkeun Oh*: Data curation, *Yu-hwa Lo & Tse Nga Ng:* Writing – review & editing, Supervision, Project administration, *Soong Ju Oh*: Conceptualization, Methodology, Investigation, Writing – review & editing, Supervision, Project administration, Funding acquition.

Conflicts of interest

There are no conflicts to declare.

Acknowledgements

B. K. J. and T. P. contributed equally to this study. This study was supported by the Technology Innovation Program(korea-led of K-Sensor technology for market leadership) (RS-2023-00256247) funded By the Ministry of Trade, Industry & Energy(MOTIE, Korea), (NRF-2018M3D1A1059001) Creative Materials Discovery Program through the National Research Foundation of Korea (NRF) funded by Ministry of Science and ICT, (2022R1A2C4001517) Basic Science Research Program through the National Research Foundation of Korea (NRF) funded by the Ministry of Science ICT and Future Planning, the National Research Foundation of Korea (NRF) grant funded by the Korean govern ment (MSIT) (No. 2022R1A2C2009523), and Samsung Electronics Co., Ltd (IO201210-08027). T. N. N. and B. S. are supported by USA National Science Foundation award ECCS-2222203.

Notes and references

The authors declare that they have no known competing financial interests or personal relationships that could have appeared to influence the work reported in this paper.

References

1 R. Sliz, M. Lejay, J. Z. Fan, M. J. Choi, S. Kinge, S. Hoogland, T. Fabritius, F. P. Garciá De Arquer and E. H. Sargent, *ACS Nano*, 2019, **13**, 11988–11995.

2 B. K. Jung, H. K. Woo, C. Shin, T. Park, N. Li, K. J. Lee, W. Kim, J. H. Bae, J. P. Ahn, T. N. Ng and S. J. Oh, *Adv Opt Mater*, 2021, **2101611**, 1–10.

3 N. Li, Y. S. Lau, Z. Xiao, L. Ding and F. Zhu, *Adv Opt Mater*, 2018, **6**, 1–9.

4 J. P. Clifford, G. Konstantatos, K. W. Johnston, S. Hoogland, L. Levina and E. H. Sargent, *Nat Nanotechnol*, 2009, **4**, 40–44.

5 K. Yang, J. Wang, Z. Zhao, F. Zhao, K. Wang, X. Zhang and F. Zhang, *Org Electron*, 2020, **83**, 105739.

6 W. Zhou, Y. Shang, F. P. García de Arquer, K. Xu, R. Wang, S. Luo, X. Xiao, X. Zhou, R. Huang, E. H. Sargent, Z. Ning, L. Wu, R. R. Xu, G. Yao, D. Su, Z. Su, H. Yang, K. Yang, J. Wang, Z. Zhao, F. Zhao, K. Wang, X. Zhang, F. Zhang, K. Xu, L. Ke, H. Dou, R. R. Xu, W. Zhou, Q. Wei, X. Sun, H. Wang, H. Wu, L. Li, J. Xue, B. Chen, T. C. Weng, L. Zheng, Y. Yu, Z. Ning, Z. Zhao, J. Wang, C. Xu, K. Yang, F. Zhao, K. Wang, X. Zhang and F. Zhang, *Org Electron*, 2020, **63**, 366–373.

7 Z. Zhao, J. Wang, C. Xu, K. Yang, F. Zhao, K. Wang, X. Zhang and F. Zhang, *Journal of Physical Chemistry Letters*, 2020, **11**, 366–373.

8 J. Zhang, M. A. Itzler, H. Zbinden and J. W. Pan, *Light Sci Appl*, 2015, **4**, 1–13.

9 Y.-L. Wu, K. Fukuda, T. Yokota and T. Someya, *Advanced Materials*, 2019, **31**, 1903687.

10 A. Rogalski, *Opto-Electronics Review*, 2012, **20**, 279–308.

11 H. Aghasi, S. M. H. Naghavi, M. Tavakoli Taba, M. A. Aseeri, A. Cathelin and E. Afshari, *Appl Phys Rev*, 2020, **7**, 21302.

12 J. Kublitski, A. Fischer, S. Xing, L. Baisinger, E. Bittrich, D. Spoltore, J. Benduhn, K. Vandewal and K. Leo, *Nat Commun*, 12, 4259 (2021).

13 J. Ahn, S. Jeon, H. K. Woo, J. Bang, Y. M. Lee, S. J. Neuhaus, W. S. Lee, T. Park, S. Y. Lee, B. K. Jung, H. Joh, M. Seong, J. H. Choi, H. G. Yoon, C. R. Kagan and S. J. Oh, *ACS Nano*, 2021, **15**, 15667–15675.

14 J. Zhang, S. Zhang, Y. Zhang, O. A. Al-Hartomy, S. Wageh, A. G. Al-Sehemi, Y. Hao, L. Gao, H. Wang and H. Zhang, *Laser Photon Rev*, 2022, **2200551**, 1–50.

15 M. Liu, N. Yazdani, M. Yarema, M. Jansen, V. Wood and E. H. Sargent, *Nat Electron*, 2021, **4**, 548–558.

16 H. S. Gupta, A. S. K. Kumar, M. S. Baghini, S. Chakrabarti and D. K. Sharma, *IEEE Photonics Technology Letters*, 2016, **28**, 1673–1674.

17 A. I. DSouza, A. Bakulin, E. Klem, D. Temple, C. Masterjohn, E. Mei and C. Li, 2018, **1065614**, 55.

18 E. H. Sargent, *Nat Photonics*, 2012, **6**, 133–135.

19 J. H. Song and S. Jeong, *Nano Converg*, 2017, **4**, 1–8.

20 M. A. Hines and G. D. Scholes, *Advanced Materials*, 2003, **15**, 1844–1849.

21 F. P. García de Arquer, D. V. Talapin, V. I. Klimov, Y. Arakawa, M. Bayer and E. H. Sargent, *Science*, , DOI:10.1126/science.aaz8541.

22 O. Voznyy, L. Levina, J. Z. Fan, M. Askerka, A. Jain, M. J. Choi, O. Ouellette, P. Todorović, L. K. Sagar and E. H. Sargent, *ACS Nano*, 2019, **13**, 11122–11128.

23 D. Y. Kim, K. R. Choudhury, J. W. Lee, D. W. Song, G. Sarasqueta and F. So, 2011, 2109–2113.

24 J. Ahn, S. Jeon, W. S. Lee, H. K. Woo, D. Kim, J. Bang and S. J. Oh, *Journal of Physical Chemistry C*, 2019, **123**, 18087–18094.

25 B. K. Jung, W. Kim and S. J. Oh, *Journal of the Korean Ceramic Society*, 2021, **58**, 521–529.

26 N. Sukharevska, D. Bederak, V. M. Goossens, J. Momand, H. Duim, D. N. Dirin, M. V. Kovalenko, B. J. Kooi and M. A. Loi, *ACS Appl Mater Interfaces*, 2021, **13**, 5195–5207.

27 A. R. Kirmani, A. D. Sheikh, M. R. Niazi, M. A. Haque, M. Liu, F. P. G. de Arquer, J. Xu, B. Sun, O. Voznyy, N. Gasparini, D. Baran, T. Wu, E. H. Sargent and A. Amassian, *Advanced Materials*, , DOI:10.1002/ADMA.201801661.

28 H. Choi, J. G. Lee, X. D. Mai, M. C. Beard, S. S. Yoon and S. Jeong, *Scientific Reports 2017 7:1*, 2017, **7**, 1–8.

29 W. Zhou, Y. Shang, F. P. García de Arquer, K. Xu, R. Wang, S. Luo, X. Xiao, X. Zhou, R. Huang, E. H. Sargent and Z. Ning, *Nat Electron*, 2020, **3**, 251–258.

30 K. Xu, L. Ke, H. Dou, R. Xu, W. Zhou, Q. Wei, X. Sun, H. Wang, H. Wu, L. Li, J. Xue, B. Chen, T. C. Weng, L. Zheng, Y. Yu and Z. Ning, *ACS Appl Mater Interfaces*, 2022, **14**, 14783–14790.

This journal is © The Royal Society of Chemistry 20xx

Please do not adjust margins

31 J. Poppe, S. Gabriel, L. Liebscher, S. G. Hickey and A. Eychmüller, *J Mater Chem C Mater*, 2013, **1**, 1515–1524.

32 Y. Lin, M. Li, J. Xia, H. Ding, L. Xu, X. Yang and S. Li, *Cellulose*, 2021, **28**, 4211–4222.

33 A. Barroso-Bogeat, M. Alexandre-Franco, C. Fernández-González and V. Gómez-Serrano, *Arabian Journal of Chemistry*, 2019, **12**, 3963–3976.

34 J. Ke, X. Li, Q. Zhao, Y. Hou and J. Chen, *Sci Rep*, 2014, **4**, 4–9.

35 Y. Cho, B. Hou, J. Lim, S. Lee, S. Pak, J. Hong, P. Giraud, A. R. Jang, Y. W. Lee, J. Lee, J. E. Jang, H. J. Snaith, S. M. Morris, J. I. Sohn, S. Cha and J. M. Kim, *ACS Energy Lett*, 2018, **3**, 1036–1043.

36 M. Salado, L. Contreras-Bernal, L. Caliò, A. Todinova, C. López-Santos, S. Ahmad, A. Borras, J. Idígoras and J. A. Anta, *J Mater Chem A Mater*, 2017, **5**, 10917–10927.

37 H. Fang and W. Hu, *Advanced Science*, , DOI:10.1002/advs.201700323.

38 H. Lee, J. Ahn, S. Im, J. Kim and W. Choi, *Sci Rep*, 2018, **8**, 1–7.

39 J.-H. Kim, B. K. Jung, S.-K. Kim, K.-R. Yun, J. Ahn, S. Oh, M.-G. Jeon, T.-J. Lee, S. Kim, N. Oh, S. J. Oh and T.-Y. Seong, *Advanced Science*, **n/a**, 2207526.

40 H. K. Woo, M. S. Kang, T. Park, J. Bang, S. Jeon, W. S. Lee, J. Ahn, G. Cho, D. K. Ko, Y. Kim, D. H. Ha and S. J. Oh, *Nanoscale*, 2019, **11**, 17498–17505.

41 J. Z. Fan, N. T. Andersen, M. Biondi, P. Todorović, B. Sun, O. Ouellette, J. Abed, L. K. Sagar, M. J. Choi, S. Hoogland, F. P. G. de Arquer and E. H. Sargent, *Advanced Materials*, 2019, **31**, 1–8.

42 F. P. García De Arquer, A. Armin, P. Meredith and E. H. Sargent, *Nat Rev Mater*, , DOI:10.1038/natrevmats.2016.100.

43 C. Li, W. Huang, L. Gao, H. Wang, L. Hu, T. Chen and H. Zhang, *Nanoscale*, 2020, **12**, 2201–2227.

44 Y. Fang, A. Armin, P. Meredith and J. Huang, *Nat Photonics*, 2019, **13**, 1–4.